



Evolution of zincian malachite synthesis by low temperature co-precipitation and its catalytic impact on the methanol synthesis



Leon Zwiener^a, Frank Girgsdies^a, Daniel Brennecke^a, Detlef Teschner^{a,b}, Albert G.F. Machoke^b, Robert Schlögl^{a,b}, Elias Frei^{a,*}

^a Department of Inorganic Chemistry, Fritz Haber Institute of the Max Planck Society, Faradayweg 4-6, 14195, Berlin, Germany

^b Department of Heterogeneous Reactions, Max Planck Institute for Chemical Energy Conversion, Stiftstrasse 34 – 36, 45470, Mülheim an der Ruhr, Germany

ARTICLE INFO

Keywords:

Zincian malachite
Co-precipitation
Methanol synthesis

ABSTRACT

Low temperature co-precipitation enabled, for the first time, the preparation of phase pure zincian malachite precursors with Zn contents of up to 31 at.-%. The high Zn content was beneficial for maximizing the dispersion of Cu and oxygen defect sites on the ZnO surface. Further, an increase of the Zn loading from 10 to 31 at.-% doubled the specific surface areas obtained from N₂O-RFC (Reactive Frontal Chromatography) and H₂-TA (Transient Adsorption). As the Zn content was increased from 10 to 31 at.-%, the apparent activation energy for methanol formation was strongly decreased. Furthermore, water formation was reduced indicating a retardation of the rWGS in favor of methanol formation at high Zn loadings. Additionally, compared to high temperature co-precipitation, low temperature precipitated catalysts exhibited increased catalytic activities.

1. Introduction

Rising global energy demand, relying on the ongoing consumption of fossil fuels, has led to a drastic increase in atmospheric CO₂ concentration over the past century [1]. Since CO₂ has been attributed to be the main anthropogenic source of the greenhouse effect, CO₂ has become a valuable carbon source available for chemical conversion (e.g. hydrogenation). Hence, the catalytic conversion of CO₂ to value added products, particularly to methanol as a key chemical and an important feedstock for the chemical industry [2], offers a promising technique for the utilization of CO₂ [3].

Since the invention of the low-pressure methanol synthesis by ICI in 1966, the industrially applied catalyst of choice consists mainly of Cu and ZnO [2,4]. In addition, this type of Cu/ZnO-based catalyst is also applied in the low-temperature water-gas-shift reaction and methanol steam reforming [2,5]. Key features of the final catalyst involve the complex interplay of a defective Cu phase including a large surface area of Cu and a ZnO-based strong metal support interaction (SMSI) [6–8]. The maximum synergism is reached by a high dispersion of Cu and ZnO, enhancing their interfacial contact and improving the catalytic activity. A perfect distribution of Cu and Zn on the atomic scale is coupled to a phase-pure precursor synthesis concept based on co-precipitation [2,9–11]. As it has been demonstrated by a vast number of research studies on this system [12–19], the physiochemical properties of the

precursor and thus the final catalyst is crucially affected by the conditions applied during its formation. This phenomenon is termed as “chemical memory” [13]. Named after their mineral counterparts, multiple crystalline precursors can be obtained ranging from Cu-rich to Zn-rich compositions, including malachite [Cu₂(OH)₂CO₃], zincian malachite [(Cu_{1-x}Zn_x)₂(OH)₂CO₃, x≤0.27] [20] and aurichalcite [(Cu,Zn)₅(OH)₆(CO₃)₂]. A higher degree of Cu substitution by Zn than 27 at.-%, in the zincian malachite lattice was so far not accessible by synthetic procedures [21], but solely present in the naturally occurring rosasite [(Cu_{1-x}Zn_x)₂(OH)₂CO₃, 0.3 < x < 0.5] [21]. It is reported that the preferred Cu/ZnO ratios are about 70:30 for ternary Cu/ZnO/Al₂O₃ [22] and 2:1 in binary Cu/ZnO catalysts [18]. Zincian malachite, derived from crystallization during aging of the initially formed transient amorphous zincian georgeite [13,23], was identified as the most promising precursor phase for the final methanol synthesis catalyst. Due to its crystallization in the form of thin interwoven needles, a favorable highly porous meso-structure is obtained [24]. Moreover, to further increase the Cu dispersion, exceeding the critical limit of 27 at.-% Zn is highly desirable. Hitherto, increasing the Zn content leads to a phase separated precursor mixture containing zincian malachite and a Zn-rich aurichalcite by-phase. This inhomogeneous precursor structure (platelets and rods) yields a poor catalytic activity [13,18]. Generally, the process of co-precipitation is seen as an interplay of saturation, nucleation and particle growth of metastable solids. As a consequence,

* Corresponding author.

E-mail address: efrei@fhi-berlin.mpg.de (E. Frei).

it is assumed that an increased Zn-incorporation into the zincian malachite structure is also kinetically controlled and thus the appearance of Zn-rich precipitation products is expected to correlate with the precipitation temperature. In this study, we address the challenge of the limited Zn incorporation in the malachite lattice by the introduction of independent temperature variables for the initial co-precipitation and subsequent aging step. Low temperature co-precipitation at 278 K followed by a controlled increase to 338 K for further aging led to a series of mixed metal hydroxycarbonate precursors. The influence of the chosen synthesis conditions on the phase composition, Cu/Zn content in the zincian malachite phase, microstructure and resulting catalytic activity in methanol synthesis are analyzed and compared to a conventional high-temperature co-precipitation approach. All samples were thoroughly analyzed by multiple techniques including powder X-ray diffraction (XRD), X-ray fluorescence spectroscopy (XRF), thermogravimetric analysis (TGA) coupled to evolved gas analysis (EGA), temperature programmed reduction (TPR), scanning electron microscopy (SEM) and transmission electron microscopy (TEM). In addition, the specific surface areas were determined by N_2O -reactive frontal chromatography (N_2O -RFC) and H_2 -transient adsorption ($\text{H}_2\text{-TA}$).

2. Experimental

2.1. General

All reagents were purchased from commercial sources and were used without further purification. Ultrapure water was taken from a Milli-Q water treatment system (Merck Millipore) and used for all experiments.

2.2. Sample preparation

The samples were prepared by a pH-controlled co-precipitation in an automated reactor setup (LabMax, Mettler-Toledo). The proper amounts of $\text{Cu}(\text{NO}_3)_2 \times 3\text{H}_2\text{O}$ ($\geq 99\%$ Carl Roth GmbH, lot: 454,217,716) and $\text{Zn}(\text{NO}_3)_2 \times 6\text{H}_2\text{O}$ ($\geq 99\%$, Carl Roth GmbH, lot: 105,226,072) were dissolved in ultrapure water and concentrated HNO_3 (10 mL, $\geq 65\%$, Carl Roth GmbH, lot: 214,212,677) was added to obtain the metal salt solution (1.0 L, 1.0 M). An appropriate amount of precipitating agent Na_2CO_3 ($\geq 99\%$ Carl Roth GmbH, lot: 156,240,183) was dissolved in ultrapure water to obtain a 1.6 M solution. The metal salt solution was added to the partially pre-filled reaction vessel (400 mL ultrapure water) with 20 mL min^{-1} at 278 K while continuously stirring (300 rpm) within 30 min. In order to keep the pH constant at a value of 6.50, appropriate amounts of Na_2CO_3 solution were added automatically during the co-precipitation step. Next, the temperature was increased to 338 K at a rate of 1.0 K min^{-1} . After the pH-drop was observed, aging of the sample continued for 30 min. Then, the sample was filter-collected and washed for several times by suspension in ultrapure water, until the conductivity of the washing medium was below 0.5 mScm^{-1} . The solid precursors were obtained by spray drying (B-290, Büchi Labortechnik GmbH). In the case of the two $\text{Zn}_{XX\text{-HT}}$ samples, the synthesis was performed at a constant temperature of 338 K during co-precipitation and aging (75 min). Calcination in a rotating furnace (XROTATE 700, Xerion Advanced Heating GmbH) with 2 rpm at 603 K for 3 h (21% O_2/Ar , 100 mL min^{-1}) yielded the CuO/ZnO precatalysts. The final active catalyst was obtained by reduction at 523 K for 90 min in 5% H_2/Ar (100 mL min^{-1}) prior to catalytic testing.

2.3. Characterization

X-ray diffraction (XRD) measurements were performed in Bragg-Brentano geometry on a D8 Advance II theta/theta diffractometer (Bruker AXS), using Ni filtered $\text{Cu K}\alpha_{1+2}$ radiation and a position sensitive energy dispersive LynxEye silicon strip detector. The data was

analyzed by full pattern fitting according to the Rietveld method as implemented in the TOPAS software package (TOPAS version 5.0, 1999–2014 Bruker AXS). The diffraction profiles of the precursors exhibited a pronounced anisotropic peak broadening, which was satisfactorily described using a adaption of the Stephens model [25] modified for anisotropic crystallite size broadening (details see [26]). Wavelength dispersive X-ray fluorescence (WDXRF) measurements were performed in a S4 PIONEER (Bruker AXS) spectrometer. The 40 mm sample discs used for the measurement were obtained from the solidified glass melt of fused sample powder (100 mg), LiBr (10 mg, Fluxana) and $\text{Li}_2\text{B}_4\text{O}_7$ (8.8 g, Fluxana, $> 99.8\%$) using a Vulcan 2 MA machine (HD Elektronik). The quantification of the data was based on a 10-point reference curve. The samples' specific surface area was determined by fitting the adsorption data with the Brunauer–Emmett–Teller (BET) model [27]. The sorption data were collected from N_2 physisorption at liquid nitrogen temperature of 77 K using an Autosorb-6B2-KR (Quantachrome). Prior to measurement, the samples were degassed at 353–373 K for 2–10 h using an Autosorb Degasser setup (Quantachrome). The uncertainty of the BET values is derived by estimating a constant error of 2%. For selected samples, the pore-size distribution was determined according to the Barrett–Joyner–Halenda (BJH) method [28]. The N_2O chemisorption capacity was determined by applying the reactive frontal chromatography (RFC) based on the method proposed by Chinchen et al. [29]. For each measurement, approximately 100 mg of precatalyst (100–200 μm particle size) were placed in a U-shaped fixed bed reactor. The reduced catalyst was obtained after in-situ reduction at 523 K for 30 min in 5% H_2/Ar (80 mL min^{-1}). The sample was cooled to room temperature, followed by $\text{Cu}^\circ\text{H}_2\text{-TA}$ and purged with He, then the gas feed was switched to 1% $\text{N}_2\text{O}/\text{He}$ (10 mL min^{-1}) for the RFC. The experiment was monitored by a quadrupole mass spectrometer (QM200 Omnistar, Pfeiffer) including N_2 (m/z 28) and the delayed signal of N_2O (m/z 44). N_2 was formed due to N_2O decomposition on Cu° and probing of oxygen vacancies in ZnO surface or partly reduced zinc species of the catalyst [30,31]. The N_2 signal trace was used for the calculation of both the N_2O chemisorption capacity and the apparent Cu° surface area ($\text{SA}_{\text{N}_2\text{O}}$). The former was calculated using the $\text{N}_2\text{O}/\text{He}$ flow, and the time interval given by the two inflection points of N_2 appearance and N_2O breakthrough. The latter was derived by using a value of $1.47 \cdot 10^{19}$ atoms m^{-2} for the mean copper surface atom density and assuming a molar stoichiometry of $\text{Cu}/\text{N}_2\text{O} = 2$ (half-monolayer coverage with oxygen). The uncertainty of the $\text{SA}_{\text{N}_2\text{O}}$ values is derived by estimating a constant error of 5%. H_2 -transient adsorption measurement ($\text{H}_2\text{-TA}$) was performed based on the method introduced by Kuld et al. [30]. For each experiment, approximately 100 mg sample (100–200 μm particle size) were used. The measurement was conducted at room temperature in 5% H_2/Ar (20 mL min^{-1}) for 1 h after purging in Argon. $\text{H}_2\text{-TA}$ of all three oxidation states of the Cu/ZnO catalysts, namely the precatalyst containing CuO , the reduced sample (Cu) and the partially oxidized sample obtained after N_2O -RFC (Cu_2O) were recorded using a thermal conductivity detector (TCD) (X-stream X2GP, Emerson Process Management). For the calculation of $\text{SA}_{\text{H}_2\text{-TA}}$ it was assumed that no H_2 is adsorbed on CuO . Furthermore, the difference in area of $\text{CuO}-\text{Cu}$ and $\text{CuO}-\text{Cu}_2\text{O}$ profile integrals and a reference TPR experiment of pure CuO is needed for the quantification of consumed H_2 . Relating it to the mean copper surface atom density of $1.47 \cdot 10^{19}$ atoms m^{-2} leads to the $\text{Cu}-\text{SA}_{\text{H}_2\text{-TA}}$. The uncertainty of the $\text{SA}_{\text{H}_2\text{-TA}}$ values is derived by estimating a constant error of 5%. Thermogravimetric (TG) measurements were performed using a STA 449 C Jupiter thermoanalyzer (Netzsch) under a controlled gas atmosphere (21% O_2/Ar , 100 mL min^{-1}). The evolved gases were analyzed by a quadrupole mass spectrometer (QMS200 Omnistar, Balzers) connected via a quartz capillary heated to 313 K. Each measurement was performed using approximately 20 mg sample in a temperature range of 300–1000 K (2 K min^{-1}). Upon cooling to room temperature, the residual powder sample was further analyzed by powder X-ray diffraction. All data were analyzed including

partial TG and curve smoothing using the NETZSCH Proteus Thermal Analysis software package (Version 6.10). Temperature-programmed reduction (TPR) experiments were performed following the principles of Monti and Baker [32]. For each measurement, approximately 100 mg of sample were heated at a rate of 6 Kmin^{-1} in a fixed bed reactor to 615 K in 5% H_2/Ar (80 mL min^{-1}). The TPR profile was recorded using a thermal conductivity detector (TCD) (X-stream X2GP, Emerson Process Management). Scanning electron microscopy (SEM) images were taken on a S-4800 SEM (Hitachi) equipped with a field emission gun (FEG) system. The sample was dispersed on a conductive carbon tape (Plano). The SEM was operated at low accelerating voltage (1.5 kV) for increased resolution of the surface features of the sample. Elemental analysis was performed at elevated accelerating voltages (20 kV) using an energy dispersive X-ray spectroscopy (EDX) detector (Bruker) connected to the SEM. X-ray photoelectron spectra were recorded on selected samples. Prior to the measurement, the precatalysts were pelletized and reduced in 5% H_2/Ar at 523 K (6 Kmin^{-1}) for 30 min. After cooling to room temperature, the samples were inertly transferred to a glove box connected to the spectrometer and mounted on the sample holder. They were directly transferred from the glove box to the spectrometer chamber without air contact. The XPS spectra were recorded using non-monochromatized Al K_α (1486.6 eV) excitation and a hemispherical analyzer (Phoibos 150, SPECS). The binding energy scale was calibrated by the standard $\text{Au 4f}_{7/2}$ and $\text{Cu 2p}_{3/2}$ procedure. To calculate the elemental composition, the Cu/Zn 2p core levels and theoretical cross sections from Yeh and Lindau [33] were used.

2.4. Catalytic testing

Methanol synthesis was used as a test reaction to evaluate the catalytic performance of different materials prepared in this work. All tests were conducted in a fixed bed reactor with an inner diameter of 6 mm and equipped with a thermocouple for in-situ recording of the temperature of the catalyst. The reactor was integrated in a test-rig for continuous catalysts testing. Analysis of reactants and products was performed by using a gas chromatograph from Agilent (Model 7890 N) equipped with a TCD/FID detector, molar sieve and PlotU columns. 300 mg of the catalyst were mixed with 700 mg of SiO_2 and placed into in the reactor. A sieve fraction of 100–200 μm was used for both the catalysts and SiO_2 . Prior to actual activity measurements, the catalyst was reduced with 10 vol.-% H_2/Ar for 60 min at 523 K and using a heating rate of 1 Kmin^{-1} . The activated catalysts were tested at 40 bar and $18.75\text{ CO}_2 / 3.75\text{ CO} / 10\text{ Ar}$ and 67.5 H_2 , a GHSV of $12,000\text{ h}^{-1}$ and various temperatures (between 463 K and 523 K). The apparent activation energy calculations follow an Arrhenius approach (\ln of the rate as a function of the inverse temperature.)

3. Results and discussion

A series of samples with varying Cu/Zn molar ratios of 100:0 to 65:35 was prepared by a low temperature co-precipitation approach at a constant pH during synthesis (Fig. S1). All samples are designated according to their nominal Zn contents as given in Table 1 (i.e. the sample with a Cu-Zn ratio of 70:30 is named as Zn_30). The calcined precursors (oxides) are named as precatalysts. Two additional samples with the suffix "HT" were prepared for reference purpose applying the conventional synthesis temperature procedure (HT, 338 K).

3.1. Synthesis of the precursors

Shifting the upper limit of Zn substitution further towards the rosasite domain, the well-established conventional constant pH co-precipitation synthesis, generally applied at elevated temperatures (323–363 K [34]) is rethought and newly developed. Independent temperature variables for the initial co-precipitation and subsequent aging steps are introduced (all other parameters are kept constant, see

experimental section). Fig. 1 exemplarily shows the applied synthesis protocol for the sample series (Table 1, Fig. S2). Co-precipitation was performed at 278 K (light colored pattern, Fig. 1), followed by an incremental increase to 338 K during aging (dark colored pattern, Fig. 1). In general, co-precipitation of zincian malachite samples lead to the initial formation of a transient amorphous zincian georgeite phase, which crystallizes during the aging time in the mother liquor. This crystallization coincides with a minimum in the pH curve and a steep turbidity increase of the liquor (after around 102 min in Fig. 1) [24]. Consequently, low-temperature co-precipitation leads to the formation of amorphous Zn-rich nuclei (Fig. S3 and Fig. S4). With increasing Zn content their crystallization event (indicated by the pH drop) is shifted to a higher temperature ($x_{\text{Zn}} \leq 0.1$) respectively, later in time (72–103 min, Fig. S2). This transient process thus leads to an individual residence time of the co-precipitated material in the mother liquor for every sample. As it is a function of time and temperature (Fig. 1b), it is assumed that an increased Zn incorporation into the zincian malachite structure is kinetically controlled and leads to a metastable "oversaturated" state, represented by the Zn-rich samples and their different crystallization behavior. The period after the pH drop (defined as aging time) was kept constant.

3.2. Characterization of the precursors

Powder X-ray diffraction data were recorded for the prepared samples featuring nominal molar Cu/Zn ratios from 100:0 to 65:35 (Table 1). For the low-temperature co-precipitated samples single-phase synthetic zincian malachite is obtained up to nominal values of $x_{\text{Zn}} \leq 0.3$, as confirmed by the Rietveld fits. Exemplarily, the fit of the Zn_30 sample is given in Fig. 2. The complete set of Rietveld fits are presented in Fig. S5. The formation of an aurichalcite by-phase is solely observed in the case of the Zn_35 sample (Fig. S5f). The metal composition determined by XRF (Table 1) is close to the nominal value of each sample, yet slightly increased in respect of Zn content for the phase-pure samples. The incorporation of Zn into the malachite structure is reflected by the lattice parameters a , b , c and the monoclinic angle β and thus allows a qualitative assessment. Fig. 3 (data in Table S2) shows the incremental increase of Zn by the substitution of Cu in the (zincian) malachite structure which leads to a Vegard-type linear trend for all lattice parameters in the studied range of $0 < x_{\text{Zn}} < 0.31$. To the best of the authors' knowledge, the present amount of 31 at.-% Zn as part of the phase-pure synthetic zincian malachite reflects the highest value reported to date.

The lattice parameters a , c and β decrease with increasing Zn content, while the b -parameter increases. This overall trend applies as well for their analogues derived from the conventional synthesis procedure (co-precipitation and aging at 338 K, circles in Fig. 3{Behrens, 2010 #552}). The overall unit cell volumes of the former are slightly increased throughout the x_{Zn} range. Furthermore, the pure malachite analogue deviates even more pronouncedly from the natural occurring mineral sample, especially in respect of the lattice parameters a and c . Based on the established linear lattice parameter trends derived from the five phase-pure (zincian) malachite samples, the Zn content of the zincian malachite fraction of the biphasic sample Zn_35 was estimated. By linear regression, the overall best match is obtained for $x_{\text{Zn}}: 0.26$ (bottom filled square, Fig. 3). Interestingly, this point almost coincides with the upper limit of zinc incorporation observed for the conventional synthesis at 338 K [35]. In this work the formation of a minor aurichalcite by-phase (~5 wt.-%) is already observed for Zn_20-HT, indicating the critical amount of $x_{\text{Zn}}: 0.2$ for a conventional binary co-precipitation (Fig. S6).

It can be assumed that the expansion of the Zn incorporation into zincian malachite at 278 K is kinetically controlled and leads to a metastable "oversaturated" state, as represented by the Zn_30 sample (see also Fig. 1b). If, however, the Zn amount becomes too high, like in the Zn_35 case, the usual formation of a separate more Zn-rich aurichalcite

Table 1

Overview of all prepared samples including elemental and phase composition (XRF, XRD), averages crystallite domain sizes (XRD), specific surface area determined by N2 physisorption (SABET), N2O reactive frontal chromatography (SAN2O) and H2-transient adsorption (SAH2-TA). Apparent activation energies (EA) for CH3OH and H2O formation including an error based on the deviation of the linear fits are given as well.

Sample	Exp. [at.-%]	Phase ^a	Domain size [nm] ^b	SA _{BET} [m ² g ⁻¹]	SA _{N2O} [m ² g ⁻¹]	SA _{H2-TA} [m ² g ⁻¹]	E _A [kJmol ⁻¹]
	Cu Zn	Precursor	Precursor	Precatalyst			CH ₃ OH H ₂ O ^c
Zn_0	100 0	Mlc	15	37	36	0.3	– –
Zn_10	89.5 10.5	Zlc	11	59	70	12.2	5.6 64 ± 2.4 98 ± 2.6
Zn_20	79.3 20.7	Zlc	10	76	87	22.9	10.4 49 ± 2.1 67 ± 2.8
Zn_25	75.1 24.9	Zlc	8.4	90	95	–	– –
Zn_30	68.8 31.2	Zlc	6.7	102	116	26.0	12.3 41 ± 0.7 67 ± 1.3
Zn_35	65.6 34.4	Zlc, Aur	–	85	–	–	– –
Zn_10_HT	90.9 9.1	Zlc	33	10	67	11.8	3.0 70 ± 2.2 135 ± 3.7
Zn_20_HT	79.9 20.1	Zlc, Aur	16	51	87	22.6	5.2 50 ± 2.4 80 ± 2.9

^a malachite (Mlc), zincian malachite (Zlc), aurichalcite (Aur).

^b The crystallite domain size values of the first 20 reflections (XRD) were averaged.

^c The E_A of H₂O is determined from the overall formation rate of H₂O and is interpreted as an approximation of the rWGS reaction as unwanted side-reaction during the CH₃OH formation.

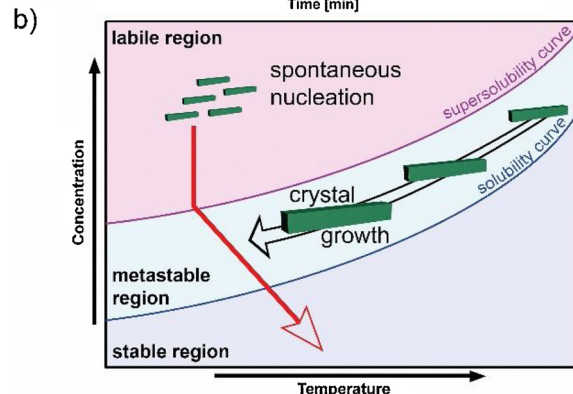
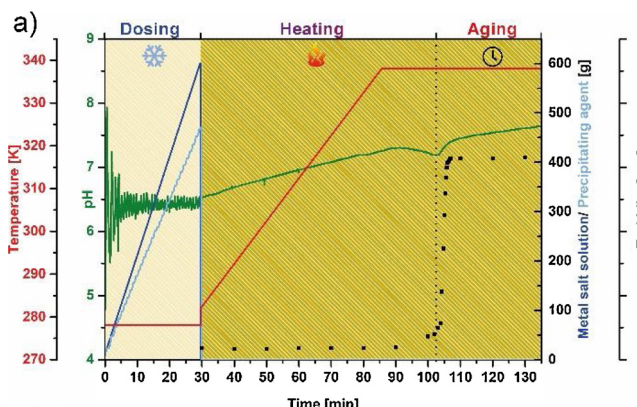


Fig. 1. Synthesis log of sample Zn_30 (a) during dosing/co-precipitation (light shaded), heating and aging time (dark shaded) including temperature (red curve), pH (green curve), turbidity (symbols), added metal salt solution (blue curve) and precipitating agent (light blue curve). Sketch of solubility- super solubility curves and corresponding occurring processes (b). Synthesis follows the red arrow's trajectory.

phase occurs. Apparently, once the aurichalcite phase forms, it provides a more favorable accommodation for the excess Zn than the over-saturated zincian malachite. Hence, the system snaps back into a more stable state which resembles the results from the conventional synthesis route. Developing another cooling/dosing recipe might lead to even more Zn-enriched synthetic malachite structures. The specific surface area determined by the BET method [27] (SA_{BET}) increases from 37 m² g⁻¹ (pure malachite sample) stepwise to its highest value of about 102 m² g⁻¹ for the Zn_30 sample (Table 1, Fig. 4). The observed trend is in accordance with the existing data in literature of conventional co-precipitated samples [36,37], but the obtained absolute values

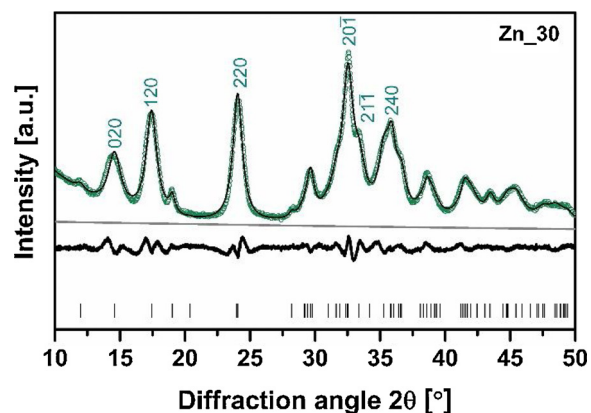


Fig. 2. Full pattern fit of the XRD pattern of synthetic zincian malachite sample Zn_30. The six most intense reflections are indexed. Experimental pattern (circles), calculated data (black line), background (grey line), difference (bottom curve) and peak positions (ticks) are given.

are exceeded. In the case of the Zn_20 sample, the determined value is increased by about 50%, when compared to its HT-analogue (Table 1). The highest measured SA_{BET} (Zn_30) is even close to the value obtained when low amounts of ternary metal ions (e.g. Al³⁺ [38]) are added to the binary Cu/Zn system [39]. In case of the Zn_35 sample, the SA_{BET} is decreased due to the presence of a binary Zlc/Aur phase mixture. Furthermore, the average anisotropic crystallite domain size decreases along both sample series (green triangles, Fig. 4). As the trends with x_{Zn} vary quantitatively for different crystal directions, the domain size values obtained for the first 20 reflections were averaged. Low-temperature co-precipitation evidently leads to the formation of smaller domain sizes, as indicated by the comparison of analogue samples of both series (e.g. Zn_10: 11 nm, Zn_10-HT: 33 nm, Table 1).

The morphology of the precursor samples was investigated by SEM analysis. The SEM micrograph of the Zn_30 sample is given in Fig. 5a. The morphology of the zincian malachite prepared at low temperature differs distinctly from the conventionally prepared samples. In the case of Zn_20, directly compared to the analogue sample prepared at 338 K (Zn_20-HT) the discrepancy in terms of the size of precipitated precursors aggregates is quite evident (Fig. S7). Low temperature formation of zincian malachite seems to lead to a less pronounced rod-like shape of the zincian malachite phase and generally to smaller aggregates. In addition, the smaller microstructure found in SEM is in line with the higher SA_{BET} found within the whole sample set and additionally in accordance with the results from XRD. The uniform elemental distribution within the sample is verified by EDX elemental mapping (Fig. S8).

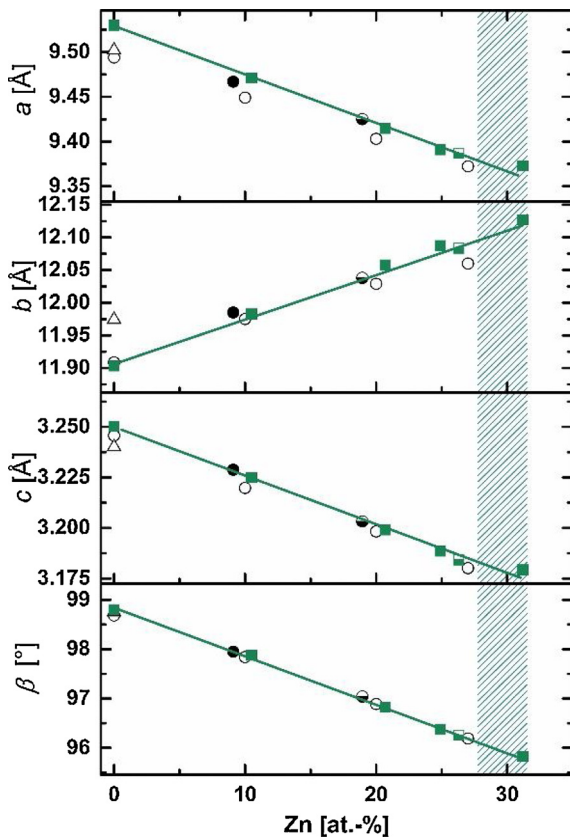


Fig. 3. Trends of lattice parameters a , b , c and β in synthetic zincian malachite as a function of Zn content. Data of phase-pure samples of this study are given as green squares (■). The estimated Zn content of the zincian malachite phase of the biphasic Zn_35 is given as a bottom filled square (■). Error bars of 3ESD (estimated standard deviations) are given but are not visible, as they are smaller than the size of the symbols used. The green hatched area highlights the increased upper limit of Zn incorporation into the zincian malachite structure. Circles (●/○) refer to zincian malachite samples prepared by the conventional synthesis route featuring co-precipitation and aging at 338 K. The estimated Zn content of the zincian malachite phase of the biphasic Zn_20-HT sample is given as bottom filled circle (●). Data for closed circles from this work and for open circles taken from [20]. Open triangles (Δ) represent the data for a mineral sample of malachite taken from [35].

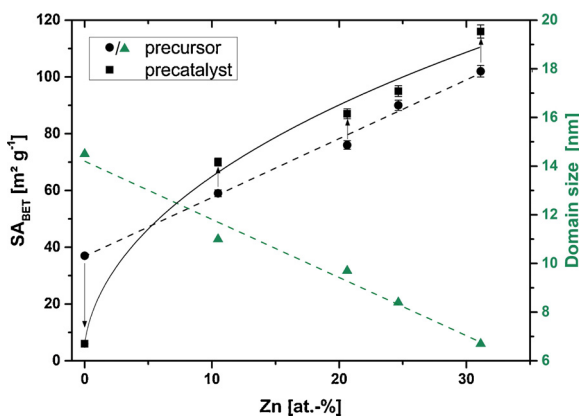


Fig. 4. BET-specific surface areas of precursor (black circle) and precatalyst (black square) samples as a function of Zn content. For the precursor samples, the corresponding average anisotropic crystallite domain sizes (green triangle) are given. Trend curves to guide the eye.

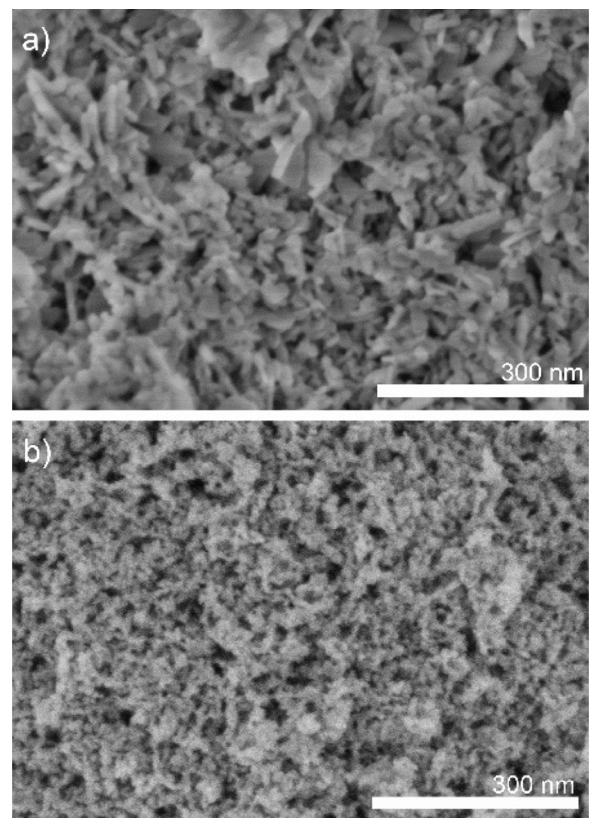
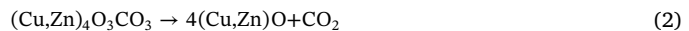


Fig. 5. SEM micrographs of zincian malachite precursor (a) and ex-zincian malachite precatalyst (b) Zn_30.

The thermal decomposition of the precursors was investigated by thermogravimetric analysis (TGA) and evolved gas analysis (EGA). During calcination, the non-substituted malachite sample decomposes in a single event [13,40] centered at around 572 K, accompanied by simultaneous H_2O (m/z 18) and CO_2 (m/z 44) release (Fig. S9a). However, two main decomposition steps are involved in the thermograms of all zincian malachite samples (Fig. S9) [13]:



Desorption of H_2O and CO_2 from the surface occurs below 400 K, followed by their concurrent liberation during the first decomposition step below 640 K (Eq. 1) accounts for a mass loss of roughly 20%. This leads to the formation of an intermediate phase $\text{M}_4\text{O}_3\text{CO}_3$ (M : Cu, Zn) which is designated as high-temperature carbonate (HT-CO₃) or anion-modified metal oxide [13,40–42]. The sole release of CO_2 during the second decomposition step at elevated temperatures above 640 K (Eq. 2) leads to its transformation into the mixed CuO/ZnO . With increasing Zn content, its stability is increased which is indicated by the thermogravimetric patterns in Fig. 6. The decomposition is associated with a mass loss of 4–8 wt.-%. Zn-rich samples contain higher amounts of HT-CO₃, yet this trend levels off for $x_{\text{Zn}} \geq 0.20$ and almost reaches the theoretical maximum (10% mass loss) [42].

3.3. Characterization of the precatalysts

All phase-pure (zincian) malachite precursors were calcined at 603 K in 21% O_2/Ar (see exp. section). The obtained black powdered samples were subsequently analyzed by X-ray diffraction to identify their phase composition. The corresponding full pattern Rietveld fits are graphically shown in Fig. S11. A decrease in crystallinity is observed for increasing Zn content within the given sample series, as

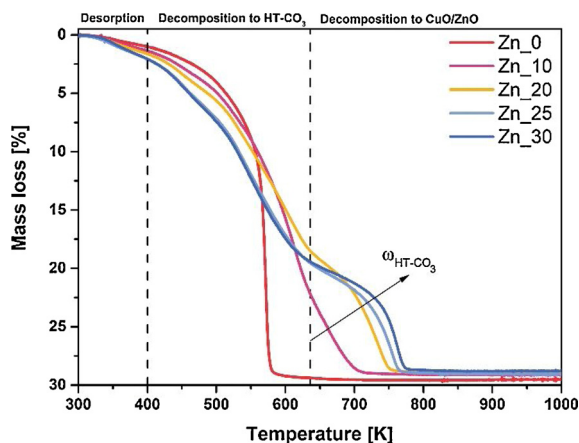


Fig. 6. Thermogravimetric decomposition patterns of prepared (zincian) malachite samples. The mass fraction ω of the HT-CO₃ rises with increasing Zn content. The stepwise decomposition of zincian malachite precursors to mixed CuO/ZnO is highlighted.

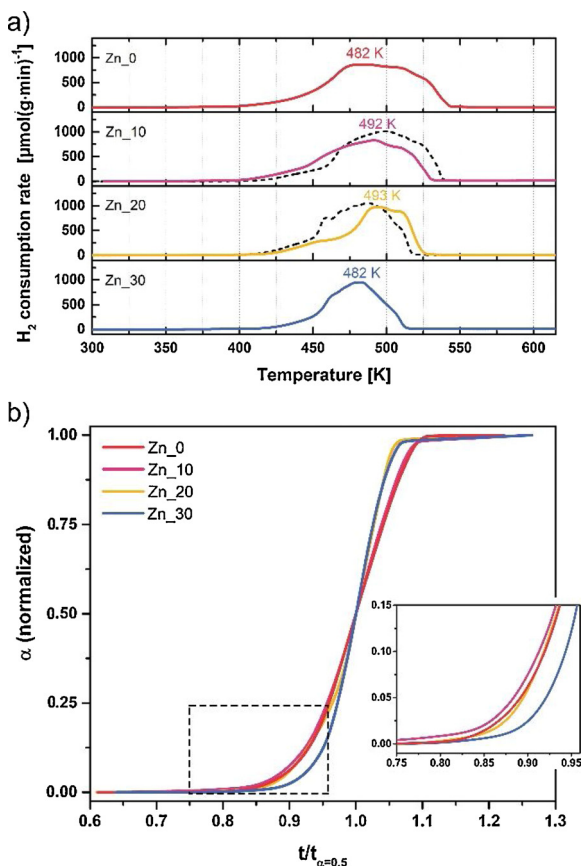


Fig. 7. TPR profiles of the precatalysts recorded at 6 K min⁻¹ in 5% H₂/Ar (a), respectively integrated TPR profiles normalized to time-fractions ($t/t_{\alpha=0.5}$) are given (b). TPR profiles of Zn_10-HT and Zn_20-HT precatalysts are given as dotted curves in Fig. 7a.

earlier described in the literature [17]. The applied thermal treatment leads to the decomposition of the initial (mixed) metal hydroxide carbonate phases yielding exclusively CuO particles in the case of the ex-malachite sample (Zn_0) and mesoporous (Fig. S14) CuO/ZnO phase mixtures in case of ex-zincian malachite samples. The former material hardly maintains its SA_{BET} after calcination, while the specific surface area of the latter sample set is further raised by up to 18% (Table 1, Fig. 4). The observed incremental increase of SA_{BET} is in line with a

decrease of Cu-content in the samples. Thus, it reaches its maximum at remarkable 116 m² g⁻¹ for the Zn_30 sample, comparable with the ternary system [39]. The given trend is in accordance with the data in literature [37]. The values obtained are of the same order of magnitude compared to the HT analogues prepared at 338 K (Table 1). The precursors' overall morphology is preserved during calcination, as confirmed by SEM analysis on, e.g., the calcined Zn_30 sample (Fig. 5b). The uniform elemental distribution within the sample is still present, as verified by EDX elemental mapping (Fig. S12). The reducibility of the aforementioned samples was investigated by temperature-programmed reduction (TPR) measurements up to 615 K in 5% H₂/Ar. The reduction profiles of the precatalysts and selected HT-analogues are shown in Fig. 7a.

The given data indicate a multi-step process which is representative for Cu-containing materials. The reduction process from Cu^{II}O to elemental Cu⁰ is known to proceed via the kinetically stabilized Cu₂O intermediate [39,43,44]. All samples are fully reduced in a temperature range between 380 K and 550 K. With increasing Zn content, the reduction temperature range narrows down to a 120 K window (Zn_30 in Fig. 7a). The maximum H₂ consumption rate of the reduction profile (T_{max}) is in the range of 487 ± 5 K for all samples. The reduction behavior is influenced by the presence of higher Zn contents in the samples as further emphasized by the presented α -plots (Fig. 7b/Fig. S15). Here, the reduction progress (α) is given as the normalized integral curve of the TPR profiles as a function of temperature (Fig. S15) and normalized to time fractions $t/t_{\alpha=0.5}$ (Fig. 7b), respectively. The samples feature an overall similar reduction behavior (Fig. 7b), which is well described by a dispersion effect of Cu steered by the Zn content. With increasing Zn content, the dispersion of Cu gets higher, reaching its climax for Zn_30, represented in a shift of the reduction start to higher temperatures (higher $t/t_{\alpha=0.5}$ value in Fig. 7b). However, the autocatalytic character of the reduction process leads to its completion already at lower temperature (lower $t/t_{\alpha=0.5}$ value in Fig. 7b) for the smaller CuO \rightarrow Cu₂O \rightarrow Cu particles.

3.4. Characterization of the catalysts

The final active catalysts were obtained after treatment of the precatalyst samples at 523 K in reductive atmosphere (5% H₂/Ar). They were characterized for their specific surface area by using N₂O-RFC and H₂-TA techniques (details see experimental section). The obtained specific surface areas are given in Table 1 and graphically presented in Fig. 8, respectively. In addition, XPS analysis was conducted to investigate the surface compositions (Table 2).

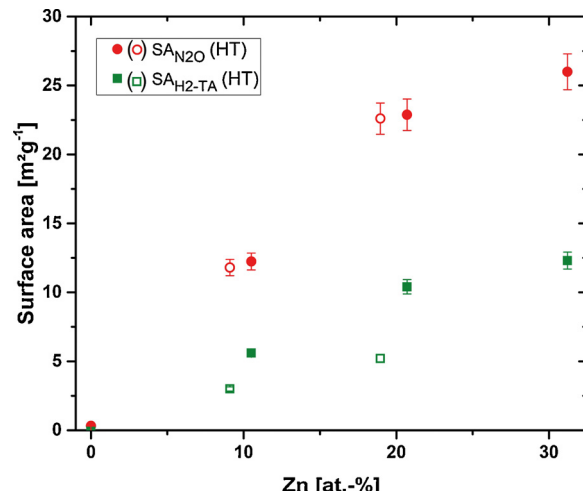


Fig. 8. Specific surface areas derived by N₂O-RFC and H₂-TA as a function of Zn content.

Table 2

Surface atomic ratios of Cu/ZnO catalysts determined by X-ray Photoelectron Spectroscopy (XPS) compared to the bulk (XRF) and nominal values.

Sample	Nominal	Bulk ^a	Surface ^b
	Zn/(Cu + Zn)	Zn/(Cu + Zn)	Zn/(Cu + Zn)
Zn_10	0.1	0.11	0.43 (291 % ^c)
Zn_20	0.2	0.21	0.54 (157% ^c)
Zn_30	0.3	0.31	0.60 (94 % ^c)
Zn_10_HT	0.1	0.09	0.40 (344 % ^c)
Zn_20_HT	0.2	0.20	0.58 (190 % ^c)

^a Determined by XRF measurements.

^b Determined by XPS analysis.

^c Quantification of Zn-enrichment at the surface based on the difference of the surface value of Zn/(Cu + Zn) (XPS) and the bulk Zn content (XRF) with respect to the bulk Zn value.

The specific surface area determined by N₂O-RFC increases with the content of Zn in the catalyst. The Zn_10 sample shows a specific surface area of about 12 m² g⁻¹, which is approximately 40 times larger compared to pure Cu alone (Zn_0: 0.3 m² g⁻¹). The increase of the Zn content leads to a further rise of the SA_{N2O} up to 23 m² g⁻¹ for Zn_20 and reaches a final value of 26 m² g⁻¹ for the Zn_30 sample. The increase of SA_{N2O} with the Zn content is already well-known in literature [37]. The HT-samples share close resemblance to the low temperature co-precipitated samples exhibiting comparable specific N₂O surface areas (Fig. 8) in line with the SA_{BET} of the corresponding precatalysts. The results imply that the addition of ZnO increases the dispersion of Cu particles and thus the present specific surface area. Besides, it is known that the N₂O-RFC technique does not solely probe the Cu surface atoms but also reacts with oxygen vacancies in ZnO_x and hence leads to an overestimation of the available Cu surface area [30,31]. Thus, to compensate for this, the specific (Cu) surface area was measured using H₂-TA as well. All obtained values determined by H₂-TA are smaller than those measured by N₂O-RFC but follow the same trend. With increasing Zn-content, the H₂-TA values increase as well, from 5.6 m² g⁻¹ (Zn_10) up to 12.3 m² g⁻¹ for the Zn_30 sample. However, when catalysts with the same nominal Zn (and Cu) content but co-precipitated at different temperatures are compared, another observation was made. About 87% higher SA_{H2-TA} was obtained for Zn_10 (5.6 vs 3.0 m² g⁻¹) and an increase by 100% is present for the Zn_20 sample (10.4 vs 5.2 m² g⁻¹), when compared to its HT analogues. Thus, HT co-precipitation leads to a high fraction of inaccessible/ covered Cu moieties.

The contribution of oxidizable defects (probably oxygen vacancies) in the ZnO surface can be calculated from the difference of the aforementioned specific surface areas. The Zn_30 sample derived by low-temperature co-precipitation i.e. accounts for oxygen vacancies of about 53% of the N₂O-RFC capacity (Zn_20 with 55%, Zn_10 with 53%). According to the low H₂-TA values of the HT-analogues of Zn_10 and Zn_20, these samples are even more rich in oxygen vacancies as

they contribute about 75% to the measured SA_{N2O}.XPS analysis provides information on the relative surface composition of the reduced samples (Table 2). An enrichment of Zn on the surface is observed for all catalysts of the two sample-series. This phenomenon is well-known in the literature and explained by the SMSI of Cu and ZnO, which leads to a partial coverage of the Cu surface by ZnO_x [7,8,39]. The relative surface enrichment of Zn decreases with the increase of the overall Zn content (bulk). But still, the highest amount is present on the surface of the reduced Zn_30 sample. Again, the Zn_10_HT (344%) and Zn_20_HT (190%) samples show a higher relative surface enrichment of Zn, which is comparable to literature values synthesized by conventional co-precipitation techniques [37]. Further, the higher surface enrichment seems to be in line with the moieties of accessible Cu and/or SA_{H2-TA}. The low-temperature synthesis approach, accompanied by a high dispersion of CuO and ZnO, leads in its reduced state to a moderately Zn-enriched surface and an equally accessible amount of freely available and covered Cu moieties (Fig. 8, Table 1). This balanced surface constitution might serve as prerequisite for an optimized Cu-ZnO interface and synergism.

3.5. Catalytic testing

Selected Cu/ZnO catalysts derived from zincian malachite precursors were tested in methanol synthesis from syngas (3.75 CO/ 18.75 CO₂/ 67.50 H₂/ 10.00 Ar) between 463 K and 503 K at 40 bar. The feed composition corresponds to the result of an Aspen® simulation at 513 K and 40 bar, considering the (r)-WGS contribution cycling back the not converted reactants. The used gas ratio mirrors an equilibrated situation at the described conditions Fig. 9 presents the evolution of the formation rates of CH₃OH and H₂O for Zn_10 (a), Zn_20 (b) and Zn_30 (c) with the reaction temperature. At any given temperature, CH₃OH formation increases with the Zn-content of the catalyst, (i.e. at 493 K, Fig. S16). This is in good agreement with the observed decrease of the apparent activation energies (E_A) of the CH₃OH formation from $64 \pm 2.4 \text{ kJ mol}^{-1}$ for the Zn_10, to $49 \pm 2.1 \text{ kJ mol}^{-1}$ for the Zn_20 and $41 \pm 0.7 \text{ kJ mol}^{-1}$ for the Zn_30. (see Arrhenius plots Fig. S17a and Table 1). Since H₂O is a by-product of the methanol formation from CO₂, its reaction rate gives valuable information about the contribution of the (reverse-) water-gas shift (WGS) reaction. Generally, H₂O formation rates lower than the CH₃OH rates are explained by the occurrence of the WGS, since feeding CO/CO₂ mixtures CO₂ is very likely the precursor for CH₃OH [45]. According to the H₂O formation shown in Fig. 9a-c, the intersection points of the formation rates mark the contribution of the rWGS reaction. It is clearly shown that with increasing Zn content the rWGS reaction is suppressed and/or shifted to higher temperatures and the WGS reaction occurs (Fig. S18). Since stable formation rates at various temperatures allow for Arrhenius plots (Fig. S17b), the E_A of the H₂O formation are also calculated (Table 1). With increasing Zn content, the E_A are decreasing. We tentatively interpreted

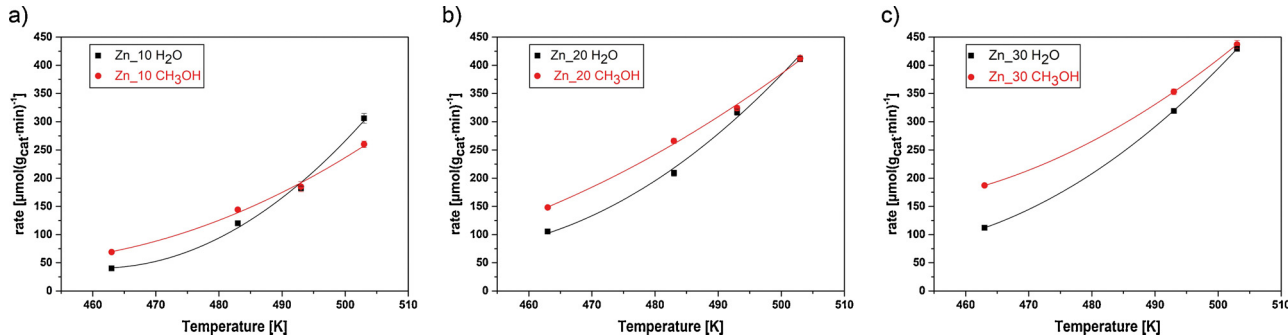


Fig. 9. Formation rates of methanol (CH₃OH) and water (H₂O) as a function of temperature and Zn-content (a–c). Data for the mixed Cu/ZnO catalysts Zn_10 (a), Zn_20 (b) and Zn_30 (c) are given. In the case of Zn_30 the catalytic testing was performed at three different temperatures. Estimated standard deviations given. Trend curves are added to guide the eye.

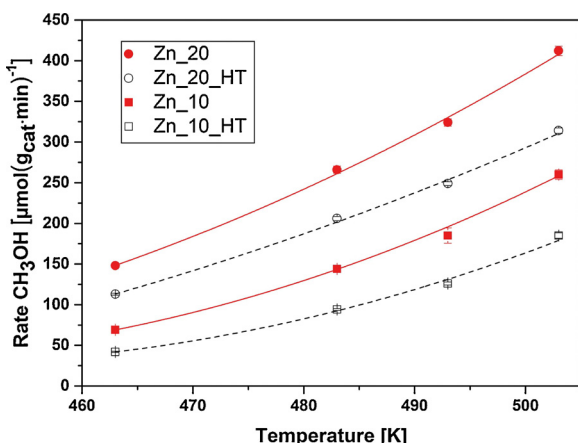


Fig. 10. Comparison of the methanol formation rates of Cu/ZnO catalysts with nominal Zn loadings of 10 and 20 at.-%, prepared by low-temperature and high temperature (HT) co-precipitation of initially mixed metal hydroxy carbonate precursors.

these values as an approximation of the (r)-WGS contribution since H₂O comes from a complex reaction network meaning high E_A of the H₂O formation (e.g. Zn_10, $98 \pm 2.6 \text{ kJ mol}^{-1}$) indicates a high activity in the rWGS reaction. This is further reflected in Table S3, where the product selectivities towards CH₃OH were calculated and e.g. the Zn_10 catalyst shows a pronounced (r)-WGS contribution. In summary, with increasing Zn content of the catalyst, the CH₃OH formation is also enhanced, while the E_A are continuously decreasing. In addition, the rWGS contribution is suppressed.

To finally judge the advantages of the low temperature co-precipitation besides the higher catalytic activity for higher Zn moieties (quantitative effect), a direct comparison of the Zn_10 and Zn_20 samples with their HT analogues is necessary. Fig. 10 shows the corresponding CH₃OH reaction rates at various temperatures. For both the Zn_10 and Zn_20 catalyst the activity is increased by 30–50 %. The calculated E_A for the CH₃OH formation are almost identical (Zn_20: $49 \pm 2.1 \text{ kJ mol}^{-1}$ and Zn_20-HT: $50 \pm 2.4 \text{ kJ mol}^{-1}$). This implies that the same kind of active sites are involved, but the number of sites is lower for the Zn_20-HT catalysts. Since the N₂O-RFC values are identical, this discrepancy is explained by the lower H₂-TA values. The almost identical values of the Cu-SA and the oxygen vacancies of the low temperature sample (as difference between N₂O-RFC and H₂-TA, see discussion above) indicate a maximization of the available Cu-ZnO interface, in agreement with the high degree of Cu dispersion. The low H₂-TA value of e.g. Zn_20-HT represents a highly covered Cu surface (by ZnO_x moieties) and thus a lower quantity of Cu-ZnO interfacial contact. Since for the rWGS and CH₃OH reaction different sites are involved, [46] the CH₃OH sites might not be strongly Zn-enriched. The E_A for water formation are increased for the HT-samples (as proxy for the rWGS contribution, Zn_20: $67 \pm 2.8 \text{ kJ mol}^{-1}$ vs Zn_20-HT: $80 \pm 2.9 \text{ kJ mol}^{-1}$), evidencing that a strongly Zn-enriched surface favors the unwanted rWGS side-reaction. Since binary Cu/ZnO catalysts are prone to a pronounced deactivation at elevated temperatures [47] (see Fig. S19a), the question arises if the differently synthesized catalysts show the same deactivation behavior. In Fig. S19b the normalized CH₃OH rates are compared at a longer time-on-stream and the activity curves decrease identically. Further, the Zn_20 catalysts were tested under industrially relevant conditions of 60 bar in syngas (Fig. S19c). Again, the Zn_20 catalyst is significantly more active than the Zn_20-HT and almost identical deactivation curves are obtained.

4. Conclusions

We herein report on a new route for the synthesis of pure Zn rich

(Cu_{1-x}Zn_x)₂(OH)₂CO₃. By the combination of low-temperature co-precipitation at 278 K and controlled aging at 338 K we obtained a series of novel zincian malachite samples. The upper limit of Zn incorporation into the malachite structure was successfully shifted up to $x_{\text{Zn}}:0.31$, the highest value reported in literature. The phase purity was verified by full-pattern Rietveld analysis on the precursors XRD data. The prepared material features small crystallite domain sizes and improved BET surface areas, which are even close to values obtained when low amounts of ternary metal ions (Al³⁺) are added to the Cu/Zn system. The precursors' morphology is drastically influenced by the developed synthesis route. In place of rod-like shaped crystallites we obtained less defined anisotropic interwoven crystallite materials. Their transformation to the corresponding CuO/ZnO precatalysts lead to an incremental increase in specific surface area, which is in line with the gain in Zn content. Thus, it reaches its climax at remarkable $116 \text{ m}^2 \text{ g}^{-1}$ for the Zn_30 sample, catching up with the ternary Cu/ZnO/Al₂O₃ system. The reduced binary catalysts feature high Cu surface areas of up to $11 \text{ m}^2 \text{ g}^{-1}$, as determined by H₂-TA. A high Zn content is desirable to further increase Cu dispersion, accordingly the highest value was observed for the Zn_30 sample. In addition, the dispersed Cu/ZnO materials are rich in (oxidizable) defects in the ZnO surface, which is expected to be favorable for catalysis. The homogeneous Cu-dispersion also leads to an equally accessible Cu surface and ZnO_x-sites, which is crucial for a maximized Cu-ZnO interface. Increased activities in methanol synthesis were measured for these binary model-type Cu/ZnO catalysts, surpassing the co-precipitated HT-analogues and suppressing the rWGS contribution. The superior activities are also preserved under industrially relevant conditions and long times-on-stream. On the basis of this model system, a further shift of the Zn content of the zincian malachite precursor phase to values above 31 at.-% is tempting. In addition, to fully exploit the potential of the presented synthesis approach, it has to be extended by another metal oxide (i.e. adapted to the industrially relevant ternary Cu/ZnO/Al₂O₃ system). Generally, this low temperature synthesis approach serves as new tool for any co-precipitated crystalline materials and catalysts.

Conflict of interest

The authors declare no conflict of interest.

Acknowledgements

The authors thank J. Allan (TG), W. Frandsen and D. Ivanov (SEM), J. Plagemann and M. Hashagen (BET) as well as Dr. O. Timpe (XRF).

Appendix A. Supplementary data

Supplementary material related to this article can be found, in the online version, at doi:<https://doi.org/10.1016/j.apcatb.2019.02.023>.

References

- W. Li, H. Wang, X. Jiang, J. Zhu, Z. Liu, X. Guo, C. Song, A short review of recent advances in CO₂ hydrogenation to hydrocarbons over heterogeneous catalysts, *RSC Adv.* 8 (2018) 7651–7669.
- J.B. Hansen, P.E. Højlund Nielsen, Methanol synthesis, *Handbook of Heterogeneous Catalysis*, Wiley-VCH Verlag GmbH & Co. KGaA, 2008, pp. 2920–2949.
- O. Tursunov, L. Kustov, A. Kustov, A brief review of carbon dioxide hydrogenation to methanol over copper and Iron Based catalysts, *oil & gas science and technology - rev, IFP Energies Nouv.* 72 (2017) 30.
- G.A. Olah, A. Goeppert, G.K.S. Prakash, *Beyond Oil and Gas: The Methanol Economy*, Wiley, 2009.
- G.C. Chinchen, M.S. Spencer, K.C. Waugh, D.A. Whan, Promotion of methanol synthesis and the water-gas shift reactions by adsorbed oxygen on supported copper catalysts, *J. Chem. Soc. Farad. Trans. 1* (83) (1987) 2193–2212.
- S. Zander, E.L. Kunke, M.E. Schuster, J. Schumann, G. Weinberg, D. Teschner, N. Jacobsen, R. Schlögl, M. Behrens, The role of the oxide component in the development of copper composite catalysts for methanol synthesis, *Angew. Chem. Int. Ed.* 52 (2013) 6536–6540.
- M. Behrens, F. Studt, I. Kasatkin, S. Kühl, M. Hävecker, F. Abild-Pedersen,

S. Zander, F. Girgsdies, P. Kurr, B.-L. Kniep, M. Tovar, R.W. Fischer, J.K. Nørskov, R. Schlögl, The active site of methanol synthesis over Cu/ZnO/Al₂O₃ industrial catalysts, *Science* 336 (2012) 893–897.

[8] T. Lunkenbein, J. Schumann, M. Behrens, R. Schlögl, M.G. Willinger, Formation of a ZnO overlayer in industrial Cu/ZnO/Al₂O₃ catalysts induced by strong metal–support interactions, *Angew. Chem. Int. Ed.* 54 (2015) 4544–4548.

[9] K. Klier, Methanol synthesis, in: H.P.D.D. Eley, B.W. Paul (Eds.), *Adv. Catal.* Academic Press, 1982, pp. 243–313.

[10] G.C. Chinchen, P.J. Deny, J.R. Jennings, M.S. Spencer, K.C. Waugh, Synthesis of methanol, *Appl. Catal.* 36 (1988) 1–65.

[11] F. Schüth, M. Hesse, K.K. Unger, Precipitation and coprecipitation, *Handbook of Heterogeneous Catalysis*, Wiley-VCH Verlag GmbH & Co. KGaA, 2008.

[12] J.L. Li, T. Inui, Characterization of precursors of methanol synthesis catalysts, copper/zinc/aluminum oxides, precipitated at different pHs and temperatures, *Appl. Catal. A Gen.* 137 (1996) 105–117.

[13] B. Bems, M. Schur, A. Dassenoy, H. Junkes, D. Herein, R. Schlögl, Relations between synthesis and microstructural properties of Copper/Zinc hydroxycarbonates, *Chem. Eur. J.* 9 (2003) 2039–2052.

[14] C. Baltes, S. Vuković, F. Schüth, Correlations between synthesis, precursor, and catalyst structure and activity of a large set of CuO/ZnO/Al₂O₃ catalysts for methanol synthesis, *J. Catal.* 258 (2008) 334–344.

[15] M. Behrens, D. Brennecke, F. Girgsdies, S. Kißner, A. Trunschke, N. Nasrudin, S. Zakaria, N.F. Idris, S.B.A. Hamid, B. Kniep, R. Fischer, W. Busser, M. Muhler, R. Schlögl, Understanding the complexity of a catalyst synthesis: co-precipitation of mixed Cu,Zn,Al hydroxycarbonate precursors for Cu/ZnO/Al₂O₃ catalysts investigated by titration experiments, *Appl. Catal. A* 392 (2011) 93–102.

[16] S.-i. Fujita, Y. Kanamori, A.M. Satriyo, N. Takezawa, Methanol synthesis from CO₂ over Cu/ZnO catalysts prepared from various coprecipitated precursors, *Catal. Today* 45 (1998) 241–244.

[17] G.C. Shen, S.-i. Fujita, N. Takezawa, Preparation of precursors for the Cu/ZnO methanol synthesis catalysts by coprecipitation methods: effects of the preparation conditions upon the structures of the precursors, *J. Catal.* 138 (1992) 754–758.

[18] D. Waller, D. Stirling, F.S. Stone, M.S. Spencer, Copper-zinc oxide catalysts. Activity in relation to precursor structure and morphology, *Farad. Discuss. Chem. Soc.* 87 (1989) 107–120.

[19] S. Zander, B. Seidlhofer, M. Behrens, In situ EDXRD study of the chemistry of aging of co-precipitated mixed Cu,Zn hydroxycarbonates - consequences for the preparation of Cu/ZnO catalysts, *Dalton Trans.* 41 (2012) 13413–13422.

[20] M. Behrens, F. Girgsdies, Structural Effects of Cu/Zn Substitution in the Malachite–Rosasite System Z, *Angew. Allg. Chem.* 636 (2010) 919–927.

[21] M. Behrens, F. Girgsdies, A. Trunschke, R. Schlögl, Minerals as model compounds for Cu/ZnO catalyst precursors: structural and thermal properties and IR spectra of mineral and synthetic (Zincian) malachite, Rosasite and Aurichalcite and a catalyst precursor mixture, *Eur. J. Inorg. Chem.* 2009 (2009) 1347–1357.

[22] M.M. Günter, T. Ressler, B. Bems, C. Büscher, T. Genger, O. Hinrichsen, M. Muhler, R. Schlögl, Implication of the microstructure of binary Cu/ZnO catalysts for their catalytic activity in methanol synthesis, *Catal. Lett.* 71 (2001) 37–44.

[23] A.M. Pollard, M.S. Spencer, R.G. Thomas, P.A. Williams, J. Holt, J.R. Jennings, Georgeite and azurite as precursors in the preparation of co-precipitated copper/zinc oxide catalysts, *Appl. Catal. A Gen.* 85 (1992) 1–11.

[24] M. Behrens, Meso- and nano-structuring of industrial Cu/ZnO/Al₂O₃ catalysts, *J. Catal.* 267 (2009) 24–29.

[25] P. Stephens, Phenomenological model of anisotropic peak broadening in powder diffraction, *J. Appl. Cryst.* 32 (1999) 281–289.

[26] X. Li, T. Lunkenbein, J. Krohnert, V. Pfeifer, F. Girgsdies, F. Rosowski, R. Schlogl, A. Trunschke, Hydrothermal synthesis of bi-functional nanostructured manganese tungstate catalysts for selective oxidation, *Farad. Discuss.* 188 (2016) 99–113.

[27] S. Brunauer, P.H. Emmett, E. Teller, Adsorption of gases in multimolecular layers, *J. Am. Chem. Soc.* 60 (1938) 309–319.

[28] E.P. Barrett, L.G. Joyner, P.P. Halenda, The determination of pore volume and area distributions in porous substances. I. Computations from nitrogen isotherms, *J. Am. Chem. Soc.* 73 (1951) 373–380.

[29] G.C. Chinchen, C.M. Hay, H.D. Vandervell, K.C. Waugh, The measurement of copper surface areas by reactive frontal chromatography, *J. Catal.* 103 (1987) 79–86.

[30] S. Kuld, C. Conradien, P.G. Moses, I. Chorkendorff, J. Sehested, Quantification of zinc atoms in a surface alloy on copper in an industrial-type methanol synthesis catalyst, *Angew. Chem.* 126 (2014) 1–6.

[31] M.B. Fichtl, J. Schumann, I. Kasatkina, N. Jacobsen, M. Behrens, R. Schlögl, M. Muhler, O. Hinrichsen, Counting of oxygen defects versus metal surface sites in methanol synthesis catalysts by different probe molecules, *Angew. Chem. Int. Ed.* 53 (2014) 7043–7047.

[32] D.A.M. Monti, A. Baiker, Temperature-programmed reduction. Parametric sensitivity and estimation of kinetic parameters, *J. Catal.* 83 (1983) 323–335.

[33] J.J. Yeh, I. Lindau, Atomic subshell photoionization cross sections and asymmetry parameters: $1 \leq Z \leq 103$, *Atom. Data Nucl. Data Tables* 32 (1985) 1–155.

[34] K.P. de Jong, *Synthesis of Solid Catalysts*, Wiley, 2009.

[35] F.J. Zigan, W. Schuster, H.D. Verfeinerung der Struktur von Malachit, Cu₂(OH)₂CO₃, Durch Neutronenbeugung, *Z. Kristallog.* 142 (1977) 412–426.

[36] Y. Okamoto, K. Fukino, T. Imanaka, S. Teranishi, Surface characterization of copper (II) oxide-zinc oxide methanol-synthesis catalysts by x-ray photoelectron spectroscopy. 1. Precursor and calcined catalysts, *J. Phys. Chem.* 87 (1983) 3740–3747.

[37] C. Álvarez Galván, J. Schumann, M. Behrens, J.L.G. Fierro, R. Schlögl, E. Frei, Reverse water-gas shift reaction at the Cu/ZnO interface: influence of the Cu/Zn ratio on structure-activity correlations, *Appl. Catal. B* 195 (2016) 104–111.

[38] M. Behrens, S. Zander, P. Kurr, N. Jacobsen, J. Senker, G. Koch, T. Ressler, R.W. Fischer, R. Schlögl, Performance improvement of nanocatalysts by promoter-induced defects in the support material: methanol synthesis over Cu/ZnO:Al, *J. Am. Chem. Soc.* 135 (2013) 6061–6068.

[39] J. Schumann, T. Lunkenbein, A. Tarasov, N. Thomas, R. Schlögl, M. Behrens, Synthesis and characterisation of a highly active Cu/ZnO:Al catalyst, *ChemCatChem* 6 (2014) 2889–2897.

[40] G.J. Millar, I.H. Holm, P.J.R. Uwins, J. Drennan, Characterization of precursors to methanol synthesis catalysts Cu/ZnO system, *J. Chem. Soc. Farad. Trans.* 94 (1998) 593–600.

[41] T.M. Yurieva, Catalyst for methanol synthesis: preparation and activation, *React. Kinet. Catal. Lett.* 55 (1995) 513–521.

[42] A. Tarasov, J. Schumann, F. Girgsdies, N. Thomas, M. Behrens, Thermokinetic investigation of binary Cu/Zn hydroxycarbonates as precursors for Cu/ZnO catalysts, *Thermochim. Acta* 591 (2014) 1–9.

[43] A. Tarasov, S. Kühl, J. Schumann, M. Behrens, Thermokinetic study of the reduction process of a CuO/ZnAl₂O₄ catalyst, *High Temp. - High Pressures* 42 (2013) 377–386.

[44] S. Kühl, A. Tarasov, S. Zander, I. Kasatkina, M. Behrens, Cu-based catalyst resulting from Cu_xZn_{1-x}Hydrotalcite-Like compound: a microstructural, thermoanalytical, and in situ XAS study, *Chem. Eur. J.* 20 (2014) 3782–3792.

[45] F. Stüdt, M. Behrens, E.L. Kunke, N. Thomas, S. Zander, A. Tarasov, J. Schumann, E. Frei, J.B. Varley, F. Abild-Pedersen, J.K. Nørskov, R. Schlögl, The mechanism of CO and CO₂ hydrogenation to methanol over Cu-based catalysts, *ChemCatChem* 7 (2015) 1105–1111.

[46] E.L. Kunke, F. Stüdt, F. Abild-Pedersen, R. Schlögl, M. Behrens, Hydrogenation of CO₂ to methanol and CO on Cu/ZnO/Al₂O₃: Is there a common intermediate or not? *J. Catal.* 328 (2015) 43–48.

[47] J. Schumann, A. Tarasov, N. Thomas, R. Schlögl, M. Behrens, Cu,Zn-based catalysts for methanol synthesis: on the effect of calcination conditions and the part of residual carbonates, *Appl. Catal. A Gen.* 516 (2016) 117–126.